Effects of Blade Fillet Structures on Flow Field and Surface Heat Transfer in a Large Meridional Expansion Turbine

Fusheng Meng *[ID]**, Qun Zheng and Jian Zhang**

College of Power and Energy Engineering, Harbin Engineering University, Harbin 150001, China
* Correspondence: B115030003@hrbeu.edu.cn; Tel.: +86-188-4612-1536

check for updates

Abstract: This paper is a continuation of the previous work, aiming to explore the influence of fillet configurations on flow and heat transfer in a large meridional expansion turbine. The endwall of large meridional expansion turbine stator has a large expansion angle, which leads to early separation of the endwall boundary layer, resulting in excessive aerodynamic loss and local thermal load. In order to improve the flow state and reduce the local high thermal load, five typical fillet distribution rules are designed. The three-dimensional Reynolds-Averaged Navier-Stokes (RANS) solver for viscous turbulent flows was used to investigate the different fillet configurations of the second stage stator blades of a 1.5-stage turbine, and which fillet distribution is suitable for large meridional expansion turbines. The influence of fillet structures on the vortex system and loss characteristics was analyzed, and its impact on wall thermal load was studied in detail. The fillet structure mainly affects the formation of horseshoe vortexes at the leading edge of the blade so as to reduce the loss caused by horseshoe vortexes and passage vortexes. The fillet structure suitable for the large meridional expansion turbine was obtained through the research. Reasonable fillet structure distribution can not only improve the flow state but also reduce the high thermal load on the wall surface of the meridional expansion turbine. It has a positive engineering guiding value.

Keywords: large meridional expansion; aerodynamic loss; thermal load; fillet configuration

1. Introduction

One of the main objectives of efficient modern gas turbine engine design is to reduce secondary flow loss at any stage. Generally speaking, the gas turbine has a higher end-wall angle design in order to achieve high-efficiency performance. The high endwall angle is designed to reduce the large deflection angle of the blade profile and meet the requirements of the expansion ratio. Due to the large expansion angle, the end-wall boundary layer separates early, resulting in a large secondary flow loss. At the same time, the thermal load of the endwall is affected by the secondary flow and becomes more complex. Numerous articles have shown that fillet structure plays an important role in reducing secondary flow loss [1,2]. However, the fillet characteristics of the large meridional expansion turbine stators have not been fully studied publicly. Therefore, it is of great value to study the influence of fillet structure on the flow and heat transfer characteristics of the large meridional expansion turbine stators.

According to Sharma et al. [3], secondary flow loss can be as high as 30%~50% in the aerodynamic loss in the stator blade row. A lot of literature shows that the detail part plays an important role in reducing the secondary loss of flow. Thole et al. [4] found that the application of an inverted circle at the junction between the leading edge of the turbine blade and the endwall could significantly weaken the horseshoe vortex. Becz et al. [5] applied an inverted circle and a bulb structure to the leading edge of a turbine cascade with a large size, a low aspect ratio, and a large angle, and found that an inverted circle

and a smaller size bulb can effectively reduce the average total pressure loss of the area, while a larger size bulb can increase the loss. It can be seen that the protruding structure of turbine blades is worthy of further study for secondary flow control. Sauer et al. [6] and Gregory et al. [7] carried out numerical simulation and experimental measurement on the blade with fillet. Results show that by modifying the leading edge, the fillet structure can reduce the secondary loss and delay the development of the passage vortex. Yan Shi et al. [8] believe that the fillet on the turbine stage is extremely effective in inhibiting the flow separation near the leading edge of the rotor blade. The mechanism of the fillet structure to reduce loss lies in that it can reduce the intensity and size of horseshoe vortexes, thus delaying the development of passage vortices [9–11]. It can be seen that shaping at the junction between the blade root and endwall, whether it is leading edge or surrounding the entire blade root, is very important for the influence of passage.

In order to improve turbine efficiency, increasing inlet temperature is a very important measure. This measure makes the first two stages of turbine blades bear higher temperature continuously, and the inlet temperature is obviously higher than the melting point of the metal. Therefore, blade cooling technology is critical. However, the prerequisite to achieve efficient and reliable cooling blade design is to fully study the characteristics of thermal load distribution of the channel and endwall without cooling structure. The fillet structure of turbine blades plays an active role in weakening the high-thermal load area of blades and endwalls. Shih et al. [12] carried out a numerical simulation study on the leading edge fillet structure of turbine blades, and the results showed that the leading edge fillet structure was helpful to reduce the heat transfer coefficient of the blade surface and endwall. Acharya [13] et al. studied the flow field and heat transfer results of different fillet structures, and found that the parabolic fillet contour was helpful to weaken the heat transfer of the endwall. Goldstein and Han et al. [14,15] used mass transfer measurements to reveal the effect of filet structure on blade heat transfer through experiments.

The flow and heat transfer characteristics of stator blades in large meridional expansion turbines have been fully described in previous studies [16], but the influence of fillet structure on it is still unclear. In this paper, the flow and heat transfer of the stator blades in the second stage of a large meridional expansion turbine is analyzed by numerical simulation with five different typical chamfered structures. The influence of fillet structures on inlet flow field structure, vortex development, and heat transfer characteristics was studied by steady-state three-dimensional Reynolds-Averaged Navier-Stokes (RANS) simulation. The experimental data was used for experimental validation. It is of engineering significance for the design of large meridional expansion turbine.

2. Numerical Methods and Validation

2.1. 5-Stage Turbine in Study and Boundary Conditions

The model studied in this paper is a 1.5-stage high-pressure turbine, including guide vanes (S1), rotor blades (R1) of the first stage, and stator blades (S2) of the second stage. The model is sufficiently extended in the inlet and outlet sections. The extension is 1.5 times the average chord length. The meridional section of the model is shown in Figure 1. It can be seen from Figure 1 that the shroud and hub endwalls of the S2 blade have an obvious large expansion angle in the meridian direction. Its average shroud expansion angle (α_1) is 22° and hub expansion angle (α_2) is 13°. The S2 blade has completed the experimental study of aerodynamic performance under low working conditions [17].
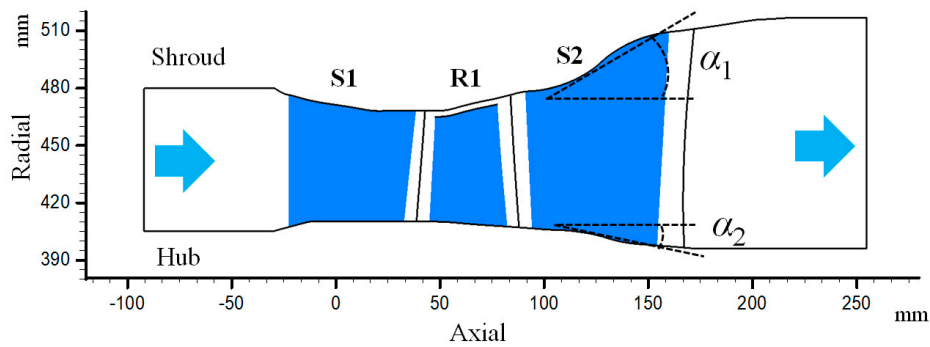
Figure 1. Meridional passage of the 1.5-stage turbine.

Detailed design parameters and working conditions of the 1.5-stage turbine are shown in Table 1. The boundary conditions at the inlet are given as the average total pressure and the average total temperature, and that at the outlet is given as the total pressure. The inlet flow angle is 0°. The hub/tip radius ratio of the blade and the mass flow rate at the design point are given. The number of blades in S1, R1, and S2 were 40, 86, and 45, respectively. The wall temperature boundary condition is set as isothermal, which can be obtained according to the temperature ratio of the mainstream gas and the isothermal wall (T_g/T_w) is equal to 1.5. The setting of this ratio was given in detail in the papers of Imran Qureshi et al. [18] and Ameni et al. [19]. It is shown in the papers that for the heat transfer simulation of turbines, the boundary conditions of non-adiabatic are usually determined by the heat transfer between the wall surface and the main flow. However, when *Nu* number is used to analyze the wall heat transfer coefficient, if the wall temperature does not change dramatically, it is generally considered to be independent of the wall temperature. Periodic boundary conditions are adopted on both sides of the channel, and the wall surfaces are set as a non-slip boundary.

Table 1. Design parameters and boundary conditions of the 1.5-stage turbine.

Parameters Name	Value
Inlet total pressure (kPa)	1947.4
Inlet total temperature (K)	1543.9
Exit static pressure (kPa)	396.7
Inlet flow angle (°)	0
Design mass flow rate (kg/s)	76.5
Inlet hub/tip radius ratio (S1,R1,S2)	0.864, 0.886, 0.863
Exit hub/tip radius ratio (S1,R1,S2)	0.886, 0.868, 0.797
Pitch at midspan (mm) (S1,R1,S2)	71, 36, 61
Number of vanes (S1,R1,S2)	40, 86, 45
T_g/T_w	1.5
T_w (K)	1030

2.2. Numerical Solver and Mesh Settings

In this paper, the turbine flow field is calculated by the high-performance commercial hydrodynamics software CFX 17.0 [20]. The software adopts the finite volume method based on the finite element method and absorbs the accuracy of the numerical solution of the finite element method. In addition, the fully implicit mesh coupling method is also used to solve the continuity equation and the momentum equation at the same time, which has good convergence performance and numerical accuracy. For the numerical calculation in this paper, Reynolds-averaged Navier-Stokes equations in generalized coordinates are solved by the finite volume space dispersion technique. The spatial discrete scheme is the "high-precision" scheme of commercial software CFX, and the time discrete scheme is the second-order backward difference Euler scheme.

This paper focuses on the detailed study of the chamfered structure on the turbine flow field and wall heat transfer, so the selected turbulence model should capture the flow state near the wall as much as possible. Meanwhile, the heat transfer coefficient of the wall is mainly determined by the flow state near the wall. Therefore, capturing the flow details near the wall is conducive to the accurate simulation of wall heat load. In the research of Krishnababu et al. [21], it is shown that the Shear-Stress Transport (SST) k-ω turbulence model has a good performance in capturing the complex flows and flow details of the turbomachine. Zuckerman et al. [22,23] carried out a detailed analysis of the turbulence models of k-ε, k-ω, SST, and v^2-f and summarized their advantages and disadvantages. The results are as follows: the SST model combines the advantages of the k-ε model and the k-ω model and has good simulation results for the whole complex flow. In addition, the SST model uses the variant equation to calculate the turbulent viscosity [24], so it has excellent results in simulating the adverse pressure gradient. Moreover, the accuracy of the SST model on the prediction of the wall heat transfer coefficient is also better than that of the k-ε and v^2-f models. So, the SST turbulence model is adopted for fluid calculation in this study.

In this paper, the turbine blade passage grid is divided by IGG/Autogrid5, a preprocessing module developed by NUMECA company for generating multi-block structured grids. Figure 2 shows the grid diagram of 1.5-stage turbines with filleted S2. Figure 3 shows the topological structure of the cross-section of the S2 blade grid model. Structural hexahedral meshes are used in all the computational meshes. In order to improve the quality of the whole computational grid, O-type grids are used for blade surface and rotor blade clearance area, and H-type grids are used for inlet and outlet areas and the mainstream area. In the paper of Montomoli et al. [25], the wall heat transfer coefficient of turbine blades were studied in detail, indicating that the use of 20-layer grids near the wall can meet the requirements for the capture of boundary layer flows and wall heat transfer. Therefore, 20 meshes are used to divide the near-wall surface meshes in this paper. The final total number of cells is 13 million. In order to meet the requirements of the SST turbulence model, the average non-dimensional near-wall distance of y plus value is less than 1, so the height of the first grid of the grid model is 0.2 μm. All the computational models in this paper adopt the same topology model and grid setup.
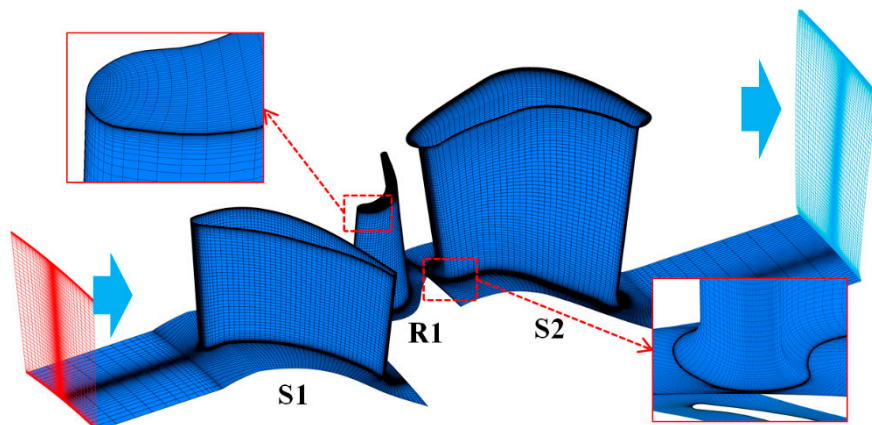

Figure 2. Schematic of computational domain of the 1.5-stage turbine.
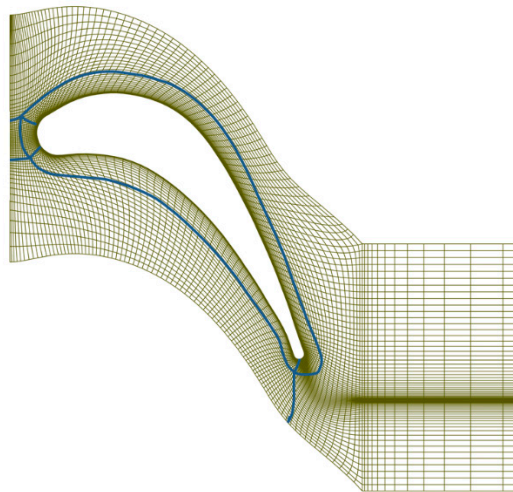
Figure 3. Blade-to-blade grid topology of stator blades (S2).

For the numerical simulation in this paper, when the residual error of the momentum equation, energy equation, and turbulence model is less than 10^{-5} orders of magnitude, and the difference between inlet and outlet flow is less than 0.1%, the calculation can be considered as convergence.

As shown in Table 2, in order to exclude the influence of the computational grid number on the aerodynamic and heat transfer results of the numerical simulation, the author conducted grid independence verification of the total pressure loss coefficient and the shroud heat flux of the model without fillet in the paper [16]. It is pointed out that when the total number of nodes in the computational grid exceeds 11 million, the numerical results are no longer dependent on the grid number. Therefore, in order to ensure that the computational grid is no longer sensitive and can accurately predict the flow characteristics near the endwall, the number of grids used in this paper is between 12 million and 13 million.

Table 2. Mesh sensitivity analysis of S2 without fillet.

	Grid Node Number (million)	C_p	Area-Averaged Shroud Heat Flux (w/m^2)
Mesh-1	3.09	0.130955	378,156
Mesh-2	7.26	0.126102	385,201
Mesh-3	11.32	0.126082	383,153

2.3. Experimental Validation of Stator Blades (S2)

In order to verify the reliability of the numerical calculation method and grid generation in this paper, aerodynamic and heat transfer tests were carried out according to the existing open experimental results. In the experimental results published so far, there is no experimental data about the transonic expansion turbine at large meridional. Therefore, this paper verifies the accuracy of numerical calculation by comparing the Mach number distribution and *Nu* number distribution results of similar blade shapes under the condition of transonic velocity. This verification has been discussed in the previous paper [16]. In the paper of Imran Qureshi et al. [18], sufficient experimental studies on aerodynamic and heat transfer related to MT1 turbine blades have been carried out, and the data are worth believing. The blade profile and turning angle of the MT1 turbine are very similar to those of the S2 blade studied in this paper, and both of them work under transonic conditions. Therefore, the verification of numerical simulation in this paper uses the experimental data made by Imran Qureshi et al. [18] on MT1 turbines. Since the S2 blade concerned in this paper is characterized by large meridional expansion, the isentropic Mach number of the blade near the shroud endwall and *Nu* distribution of the shroud endwall are compared. In the verification and simulation of the MT1

turbine, the grid model, topology, and turbulence model set are consistent with the turbine model set in this paper. Figure 4 shows the comparison of isentropic Mach number between experimental data and numerical simulation results at the position of 90% blade height. Figure 5 shows the *Nu* distribution of the circumferential mean of the upper endwall. It can be seen from Figure 4 that the numerical simulation method adopted in this paper has a good effect on the aerodynamic simulation of the near-endwall of the turbine blade. Figure 5 shows that the difference between numerical data and experimental data is 9.62% in the simulation of heat transfer. The numerical simulation method can accurately predict the heat transfer trend of the shroud. The difference between the leading edge and the trailing edge is theoretically reasonable. Therefore, the heat transfer prediction in this paper can meet the research needs. It can be seen from the above analysis that the numerical simulation method and the grid model adopted in this paper are accurate and reasonable considering the errors caused by the experiment.
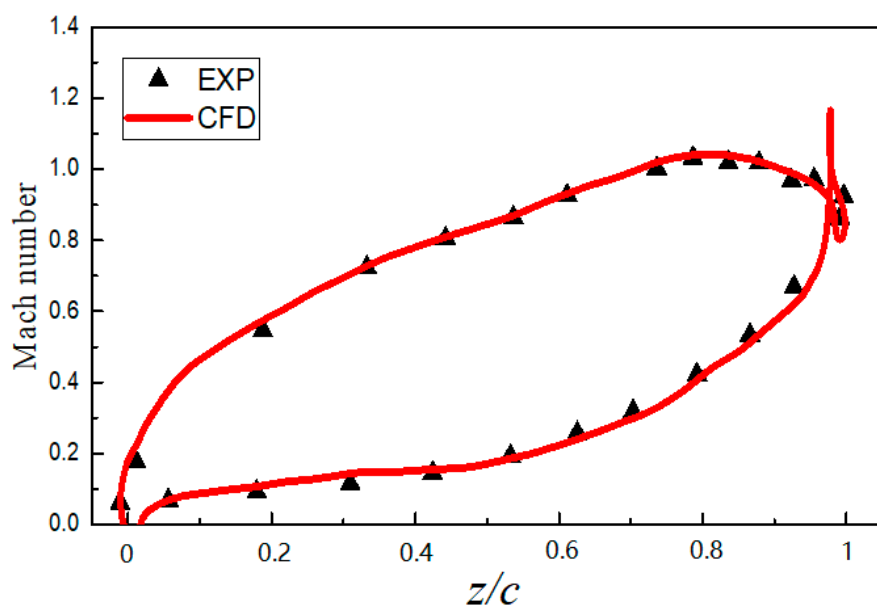

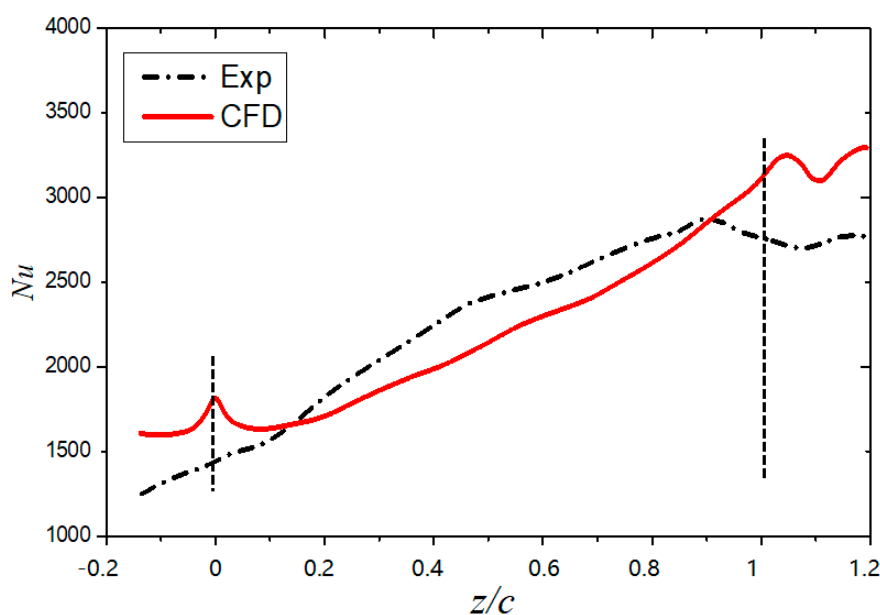**Figure 4.** Isentropic Mach number of S2 at 90% span.

Figure 5. Nu distribution of S2 shroud.

2.4. Fillet Configuration

Six different fillet structure models of S1 are designed in this paper based on the parameters fillet radius (*R*) and included an angle (*θ*). The specific design parameters are shown in Table 3. As shown in geometric design Figure 6 for fillet, a chamfering circle is not completely tangent to the endwall but has a minimum *θ* to rearrange itself in the wall. When the fillet and endwall are completely tangent, it will cause a sharp decline in the grid orthogonality near the endwall, which can lead to producing a very big error in the process of numerical simulation. For this reason, *θ* is set to 10° in this article. Therefore, in the setting of the grid structure, the fillet is determined by two parameters. When the *R* changes along the axis, there are five representative trends, that is, the radius size is constant along the axis, monotone minus, monotone increase, first decrease then increase, first increase then decrease. Therefore, this paper designs five types of fillet and non-fillet blades, which are circular structures at the root and the top. At the same axial position, the radius of the suction pressure surface is the same, that is, the distribution is symmetric. At present, there is no uniform regulation on the limitation of the blade fillet radius, but due to the limitation of channel size, the radius cannot be enlarged indefinitely. According to the existing literature, the largest radius of the fillet in the blade is in the research of the Becz et al. [5], and in the turbo blade, the maximum radius is about 25% of the width of the throat. When the radius of the blade root rounding continues to be enlarged, in practical applications, the flow loss of the blade will rise sharply, which is unfavorable to the aerodynamic performance of the engine. Therefore, the sum of the radius of the suction surface and pressure surface at the same axial position shall not exceed 50% of the minimum width of the cascade channel. That is, the radius size relationship is determined by the following formula:

$$R_{\mathrm{ps}}\big|_z + R_{\mathrm{ss}}\big|_z \leq \frac{t_{\min}\big|_z}{2} \tag{1}$$

where, the subscripts ps, ss, min, and *z* respectively represent the pressure surface, suction surface, minimum value, and an axial position, and t represents the channel width of the cascade.

$$R \leq \frac{t_{min}}{4} \tag{2}$$

Table 3. Fillet configuration parameters and codes.

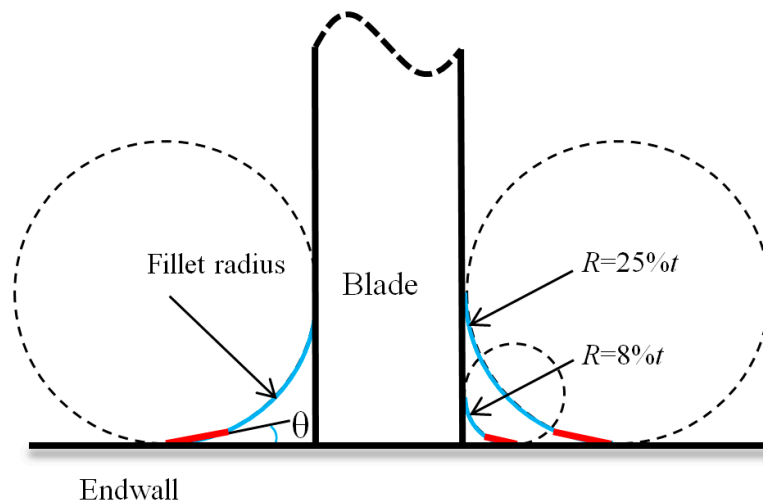| Schemes	Parameter Setting	Value (mm)	Code
Case1	$R = 0\%\ t$	0	$R1 = 0\%\ t$
Case2	$R = 25\%\ t$	6	$R2 = 25\%\ t$
Case3	$R(\mathrm{LE}) = 25\%\ t$	6	$R3 = (25\text{–}8)\%\ t$
	$R(\mathrm{TE}) = 8\%\ t$	2	
Case4	$R(\mathrm{LE}) = 8\%\ t$	2	$R4 = (8\text{–}25)\%\ t$
	$R(\mathrm{TE}) = 25\%\ t$	6	
Case5	$R(\mathrm{LE}) = 25\%\ t$	6	$R5 = (25\text{–}8\text{–}25)\%\ t$
	$R(\mathrm{MD}) = 8\%\ t$	2	
	$R(\mathrm{TE}) = 25\%\ t$	6	
Case6	$R(\mathrm{LE}) = 8\%\ t$	2	$R6 = (8\text{–}25\text{–}8)\%\ t$
	$R(\mathrm{MD}) = 25\%\ t$	6	
	$R(\mathrm{TE}) = 8\%\ t$	2	

Figure 6. Design parameters: fillet radius and minimum angle.

According to the limitation of formula (2), *R* is calculated to be less than 6 mm, and the maximum radius is about 1/2 of the thickness of the inlet boundary layer. In this paper, according to the actual processing requirements, the minimum *R* is selected as 8% *t*, and the value is equal to 2 mm.

Figure 7 shows the distribution diagram of 6 typical fillets (each form has numerous distributions, but the mechanism of the influence on the flow field is similar, which will be analyzed below and the reasons will be given). The curve represents the projection of the inverted circle contour on the meridian plane, the abscissa is axial, the starting point and ending point correspond to the leading edge (LE) and trailing edge (TE) of the S2 respectively, and the ordinate is radial. Figure 8 shows the three-dimensional (3D) schematic diagram of 6 cases, which is conducive to a better understanding of their distribution rules.
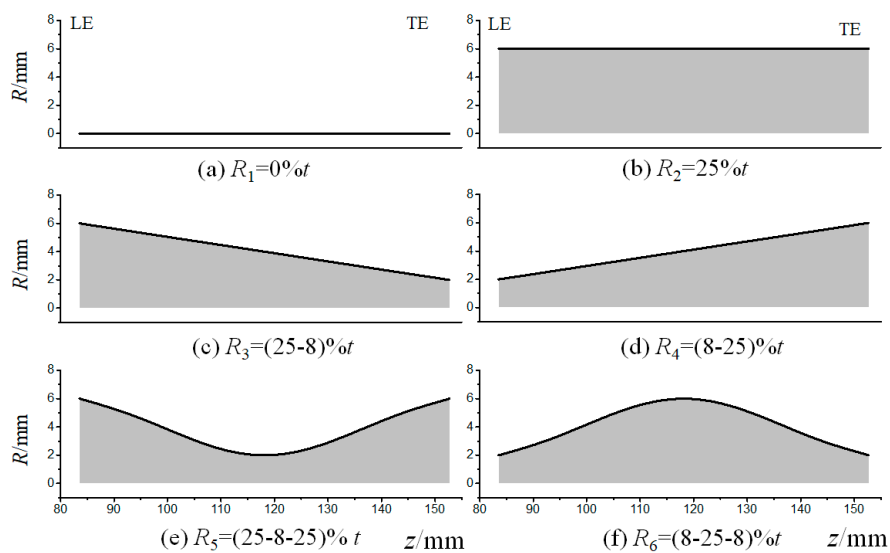

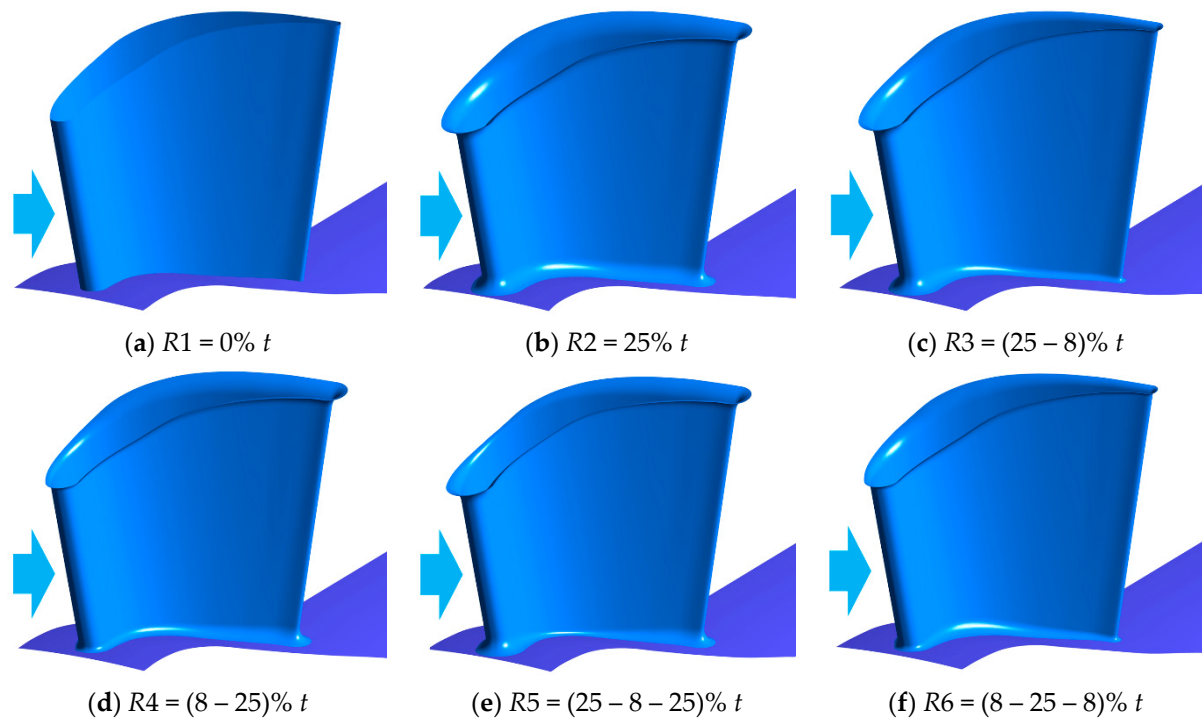**Figure 7.** Radius distribution of six different fillet structures.

(**a**) $R1 = 0\% \ t$ (**b**) $R2 = 25\% \ t$ (**c**) $R3 = (25 - 8)\% \ t$

(**d**) $R4 = (8 - 25)\% \ t$ (**e**) $R5 = (25 - 8 - 25)\% \ t$ (**f**) $R6 = (8 - 25 - 8)\% \ t$

Figure 8. Three-dimensional (3D) schematic diagram of S2 with fillet.

3. Results and Analysis

3.1. Aerodynamic Analysis of S2 with Different Fillet Structures

The formation of the horseshoe vortex (HV) at the leading edge of the blade is first affected by the fillet structure. Figure 9 is the limiting flow diagram at the hub of the S2 leading edge, showing the position and structure of HV. Results show that the HV at the leading edge is only affected by R of the leading edge fillet and not by the downstream structure of the fillet. The fillet influences the radial development of HV at the leading edge. With the increase of R at the leading edge, HV develops upward along the fillet and is closer to the blade. This change is due to the concavity of the fillet surface, which results in a low acceleration of the flow. This reduces the intensity of the adverse pressure gradient applied by the leading edge of the blade, which is the main driving force for the formation of HV. In addition, it leads to a decrease in the shape of the passage vortex (PV), which will be discussed in the next section.
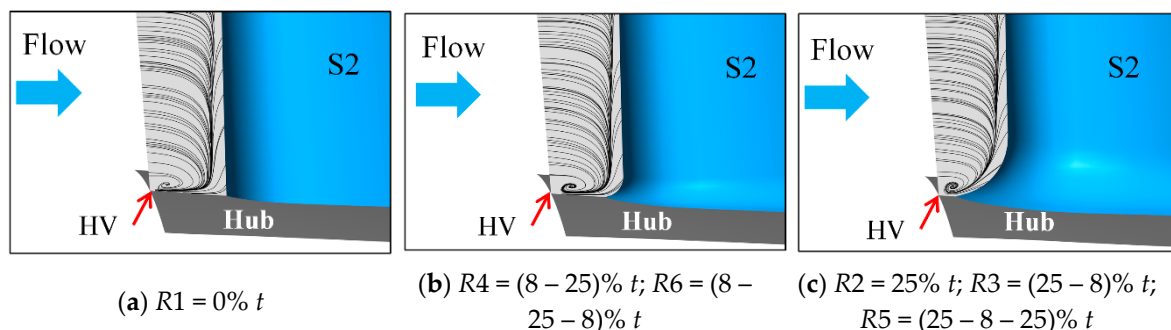

(**a**) $R1 = 0\% \ t$ (**b**) $R4 = (8 - 25)\% \ t; R6 = (8 - 25 - 8)\% \ t$ (**c**) $R2 = 25\% \ t; R3 = (25 - 8)\% \ t; R5 = (25 - 8 - 25)\% \ t$

Figure 9. Horseshoe vortex structure at the leading edge of S2.

For the static pressure coefficients (C_{ps}) at different blade heights, the load distribution and aerodynamic performance of the blades can be well expressed. The blade profile load distribution of the turbine blade directly affects the intensity of downstream secondary flows (Marchal and Sieverding et al. [26] and Benner et al. [27]).

Figure 10 shows the pressure distribution of the 1%, 50%, and 99% blade height of S2, in which the positions of 1% and 99% blade height are located on the fillet structure. The magnitude of the adverse-pressure region of the suction surface is represented by h, and a histogram is drawn. Combined with Figure 10a–c, it can be seen that the fillet structure only affects the pressure distribution near the endwall but has little impact on the middle of the blade height. Therefore, the research in this paper focuses on the vicinity of the endwall. Combined with Figure 10a,c, it can be seen that fillet mainly affects the pressure distribution of the front half of the blade suction and the trailing edge of the pressure surface. When $R = 25\% t$ of the leading fillet radius is compared with $R = 8\% t$, the adverse-pressure region decreases by about 50%. So the large leading fillet radius is helpful to improve the flow state of the suction surface. Near the trailing edge of the pressure surface, the small fillet radius ($R = 8\% t$) is used to reduce the fluctuation, so as to improve the outlet flow state of the near endwall.
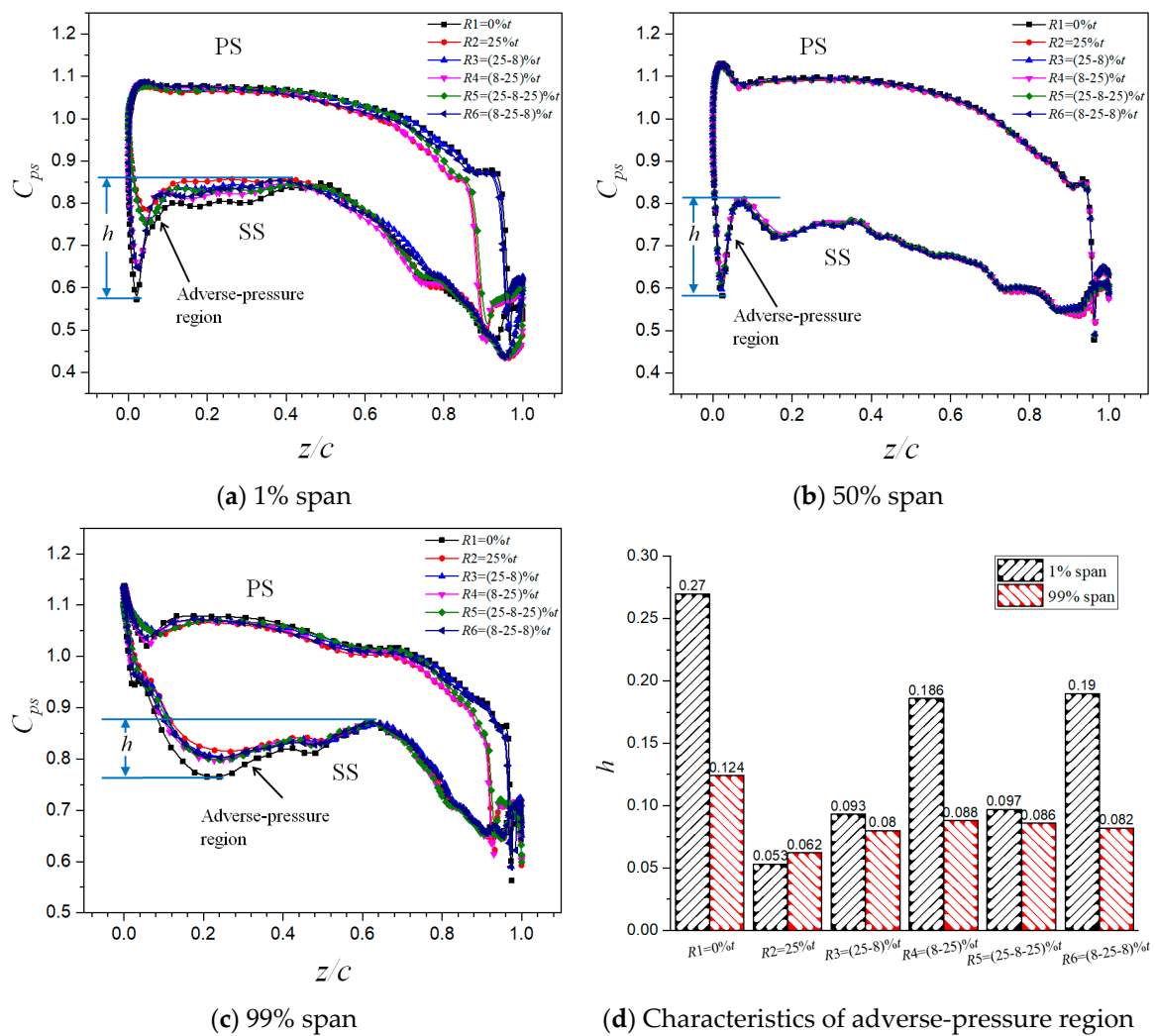

(**a**) 1% span

(**b**) 50% span

(**c**) 99% span

(**d**) Characteristics of adverse-pressure region

Figure 10. C_{ps} distribution for S2 at 1% span (**a**), 50% span (**b**), and 99% span (**c**) blade and characteristics of adverse-pressure region (**d**).

The relative total pressure loss coefficient is defined as:

$$Y_P = \left(\bar{p}_{t,in} - p_t\right)/\left(\bar{p}_{t,in} - \bar{p}_{s,out}\right) \tag{3}$$

where, $\bar{p}_{t,in}$ is the average relative total pressure at the inlet of S2, p_t is local relative total pressure, and $\bar{p}_{s,out}$ is the average static pressure at the outlet of S2.

The fillet structure initially affects the development of HV at the leading edge of the blade. Therefore, Figure 11 shows the development charts of HV and PV at the leading edge and channel under the six chamfered structures. The HV$_{PS}$ and HV$_{SS}$ of the S2 are clearly visible, where they flow downstream and form a strong PV after the intersection of the suction surface. According to Figure 11b,c,e, the leading edge radius $R = 25\% \, t$ is conducive to the reduction of HV$_{PS}$ and PV. With the increase of R in the middle of the channel, the attachment position of HV$_{SS}$ on the suction surface moves up and its strength decreases. Therefore, a larger R is adopted in the middle of the channel, which is conducive to improving the local flow of the suction surface.

(**a**) $R1 = 0\% \, t$　　　　　　(**b**) $R2 = 25\% \, t$　　　　　　(**c**) $R3 = (25 - 8)\% \, t$

(**d**) $R4 = (8 - 25)\% \, t$　　　　(**e**) $R5 = (25 - 8 - 25)\% \, t$　　　　(**f**) $R6 = (8 - 25 - 8)\% \, t$
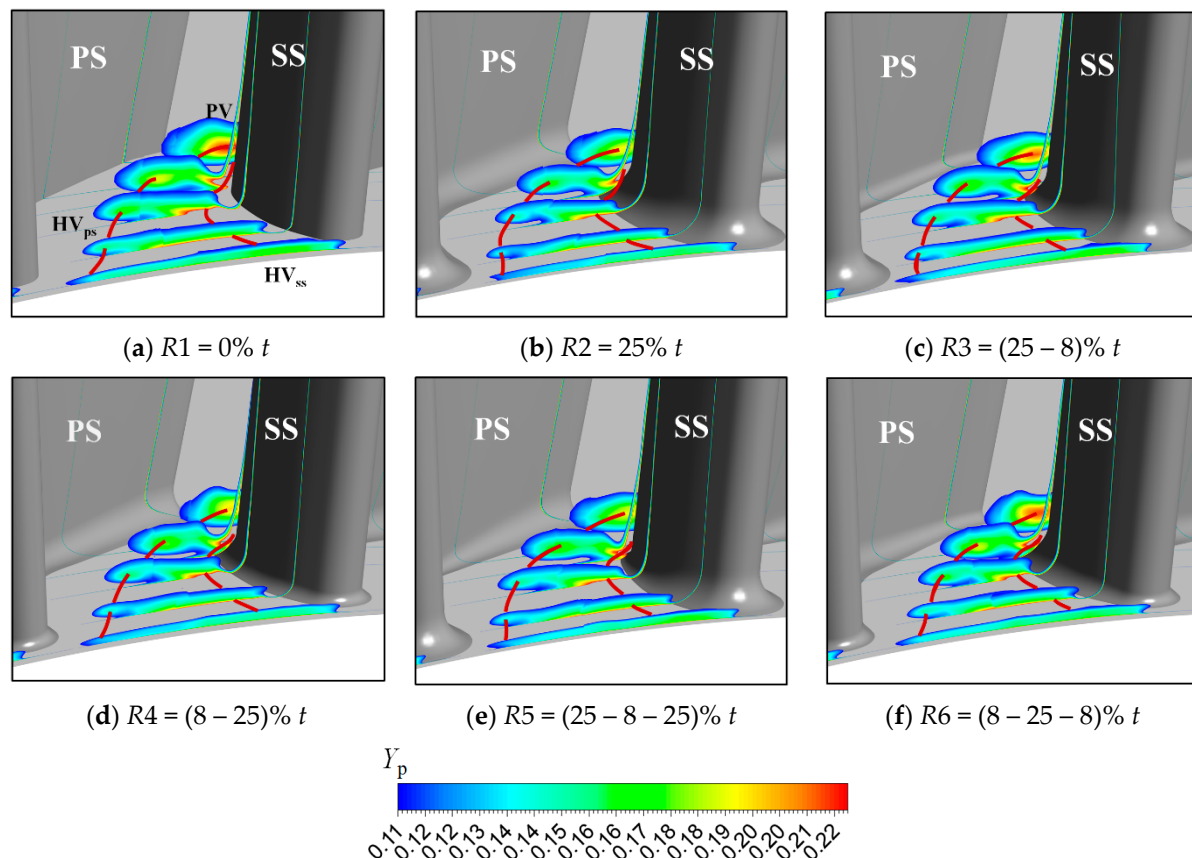
Figure 11. Horseshoe vortex imposed with relative total pressure loss coefficient.

In order to illustrate the influence of the fillet structure on shed vortices and passage vortices, Figure 12 shows the entropy-increase isoline at 110% axial chord length of S2. As can be seen from Figure 12a–f, the fillet mainly affects the flow loss at the outlet near the hub but has little impact on the other parts of the blade. Compared with the case without fillet in Figure 12a, the large radius fillet ($R = 25\% \, t$) significantly increases the shed vortex (SV) loss at the outlet near the hub. The SV loss at the hub position at the outlet can be significantly reduced by using the appropriate small radius fillet ($R = 8\% \, t$) at the blade trailing edge. Therefore, the appropriate small radius fillet at the outlet of the blade is helpful for improving the flow state. In order to quantitatively compare the loss changes at the outlet from the numerical perspective, Figure 13 shows the entropy-increase curves after the circumference average. While the fillet structure mainly affects the loss near the hub, it also affects the loss of SV and PV at the exit. As can be seen from the partial magnification, the loss of the SV and PV is increased by the enlargement of the fillet radius. At the same time, fillet structures also affect the radial position of the vortices. The loss near the shroud at the exit was reduced by about 8% by using large radius fillet ($R = 25\% \, t$) at the trailing edge. However, it increased the loss near the hub by 9%.
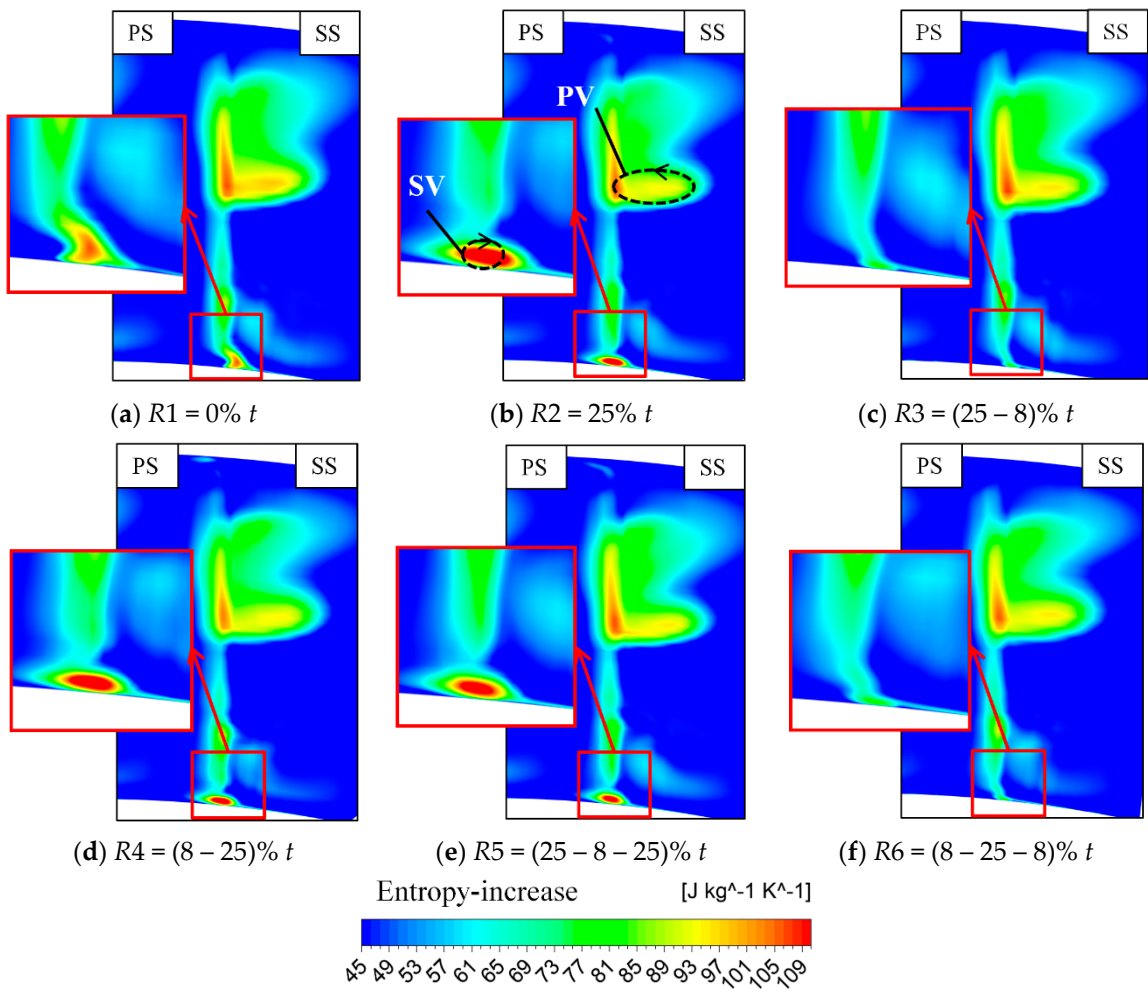
(**a**) *R1* = 0% *t*   (**b**) *R2* = 25% *t*   (**c**) *R3* = (25 − 8)% *t*

(**d**) *R4* = (8 − 25)% *t*   (**e**) *R5* = (25 − 8 − 25)% *t*   (**f**) *R6* = (8 − 25 − 8)% *t*

Figure 12. Entropy-increase isoline at 110% axial chord length of S2.
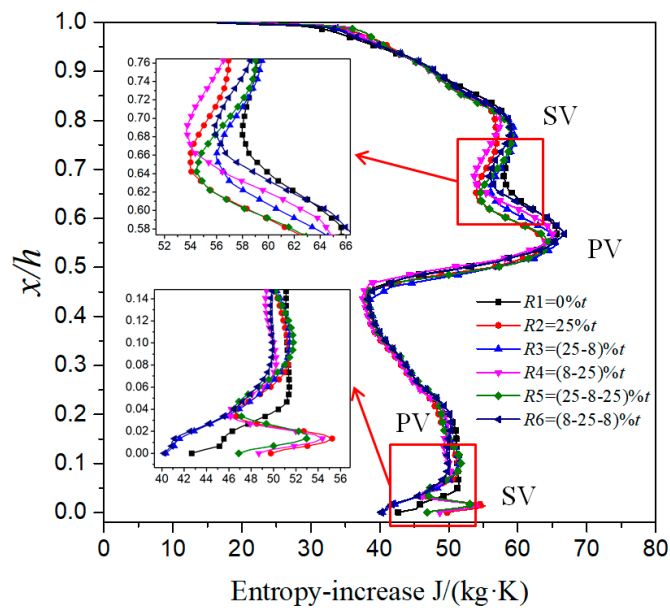

Figure 13. Radial distribution of entropy-increase at 110% axial chord length of S2.

3.2. Heat Transfer Analysis of S2 with Different Fillet Structures

The heat transfer of the wall surface can be expressed by the Nusselt number (*Nu*). *Nu* is the dimensionless heat transfer coefficient. This working with Salvadori Simone et al. [28] and Imran Qureshi et al. [18] research defined the same, is defined as:

$$Nu = \frac{\dot{q}C}{(T_{aw} - T_w)k_{T01}} \tag{4}$$

where, the parameter $\dot{q}$ is the heat flux, C is the average chord length of blades, k_{T01} is the thermal conductivity of the air referring to the average total inlet temperature.

According to the flow performance analysis, as the shroud expansion angle of the S2 is larger, the flow separation caused by it is more serious. Therefore, Figure 14 shows the *Nu* distribution of the S2 shroud. The maximum thermal load area (a) of the shroud is located at the leading edge of the blade, which is caused by the saddle point of the airflow at the leading edge. In the rear part of the suction surface, due to the separation of airflow, there is a minimum thermal load area (b). The relatively high thermal load area is located at the rear part of the pressure side (c). In the trailing edge part, due to the influence of trailing edge shedding vortexes, there is a local high thermal load area (d). Combined with Figure 14a–f, it can be easily seen that the existence of the fillet structure can significantly eliminate the maximum thermal load area (a). Whether it increases the thermal load at the leading edge fillet will be discussed in the next section. Fillet structure has little effect on regions (b) and (c). It can be seen from Figure 14c,f that appropriate small radius fillet ($R = 8\%\ t$) at the trailing edge can eliminate the local high thermal load area (d). However, if the fillet radius of the trailing edge is too large ($R = 25\%\ t$), the heat transfer coefficient of the area (d) will be significantly increased.
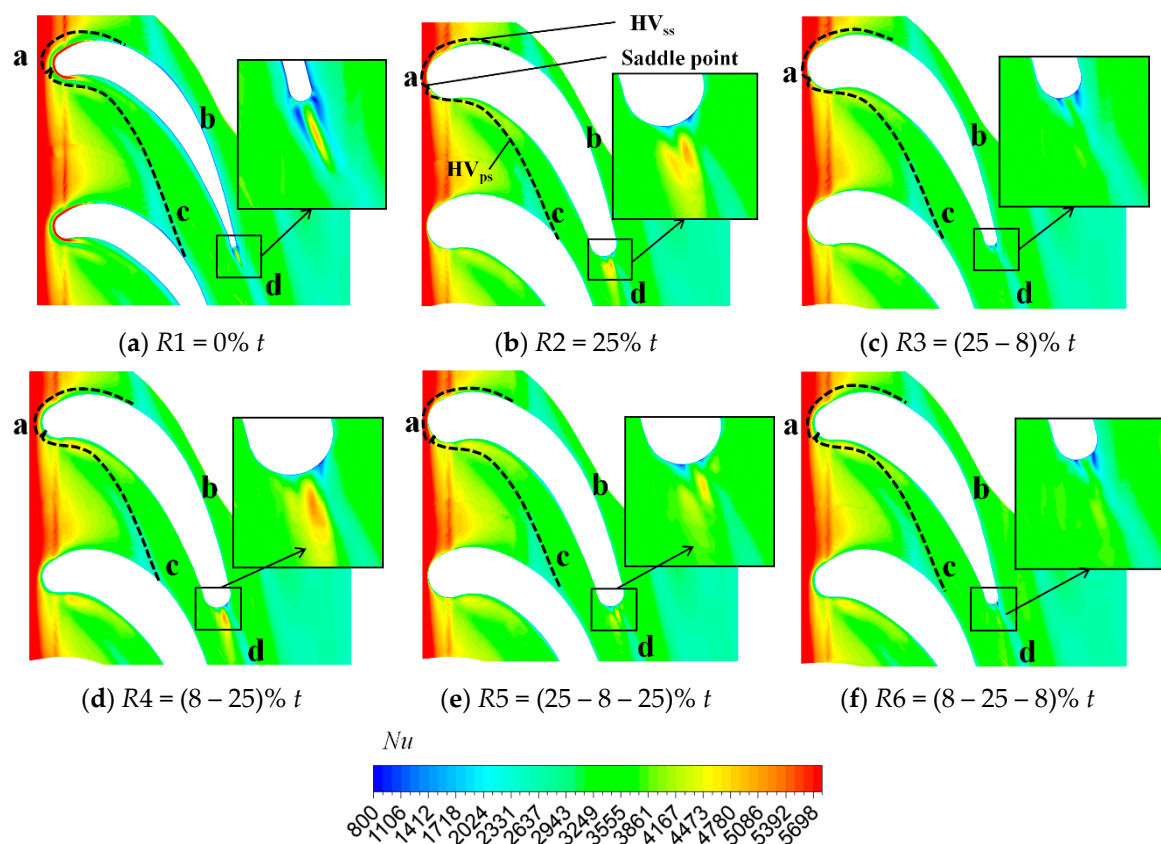

Figure 14. Distribution of *Nu* of shroud endwall of S2.

In order to further study the influence of fillet structure on the thermal load distribution on the blade surface, Figure 15 shows the *Nu* distribution of the S2 suction surface with different fillet structures. Since it has little influence on the thermal load on the pressure surface, the *Nu* distribution on the pressure surface is not given. It can be clearly seen from Figure 15a that the high thermal load area of the blade is located on the suction surface near the shroud, which is jointly caused by the passage vortex and the upstream leakage vortex. As can be seen from Figure 15b,c,e, the high thermal load area (PV region) on the suction surface can be significantly weakened by the use of large radius fillet (*R* = 25% *t*) at the leading edge of the blade. And the SV separation position will be postponed correspondingly. However, the fillet with a small radius (*R* = 8% *t*) at the leading edge does not reduce the high thermal load area (PV region). The variation laws of the fillet along the chord length and the radius of the fillet at the trailing edge have little influence on the distribution of thermal load on the blade surface.
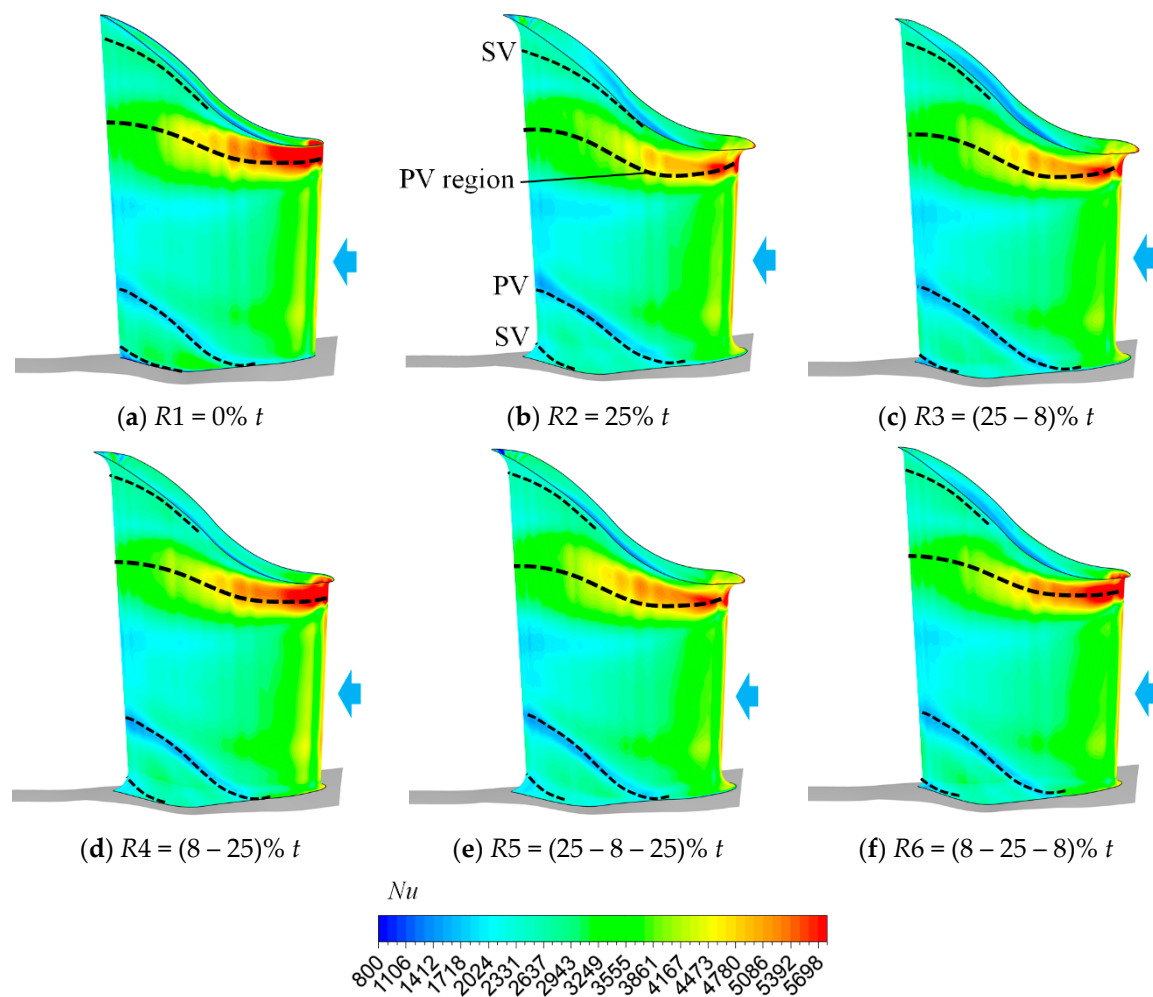

(a) *R*1 = 0% *t*　　　　**(b)** *R*2 = 25% *t*　　　　**(c)** *R*3 = (25 − 8)% *t*

(d) *R*4 = (8 − 25)% *t*　　　**(e)** *R*5 = (25 − 8 − 25)% *t*　　　**(f)** *R*6 = (8 − 25 − 8)% *t*

Figure 15. *Nu* distribution of the S2 blade suction surface.

In order to more accurately show the influence of the fillet on the heat transfer coefficient distribution of the blade surface, *Nu* distribution of three blade sections (90% span, 50% span, and 10% span) is drawn in Figure 16. Through the analysis of Figure 16a–c, it can be concluded that fillet mainly affects *Nu* distribution of the suction surface near the shroud and hub of the blade, but has little influence on the middle part of the blade. The maximum thermal load on the blade surface is located at the leading edge of the S2, 2.5 times of the average heat load. As can be seen from Figure 16a, at the position of 90% span sections of the S2, the thermal load on the suction surface is significantly higher than that on the pressure surface, which is twice as high. The maximum thermal load can be reduced by

about 28% by using the large radius fillet ($R = 25\%\ t$) at the leading edge of the S2. In addition, a large radius fillet ($R = 25\%\ t$) designed in the middle of the blade chord length can reduce the heat load on the suction surface. At the trailing edge of the blade, the fillet structure has no obvious influence on the heat load distribution. As can be seen from Figure 16c, fillet structure has little influence on the maximum heat load near the hub region but has a great influence on its fluctuation on the suction surface. Similarly, large radius fillet ($R = 25\%\ t$) in the middle of blade chord length is conducive to reducing the thermal load near the hub.
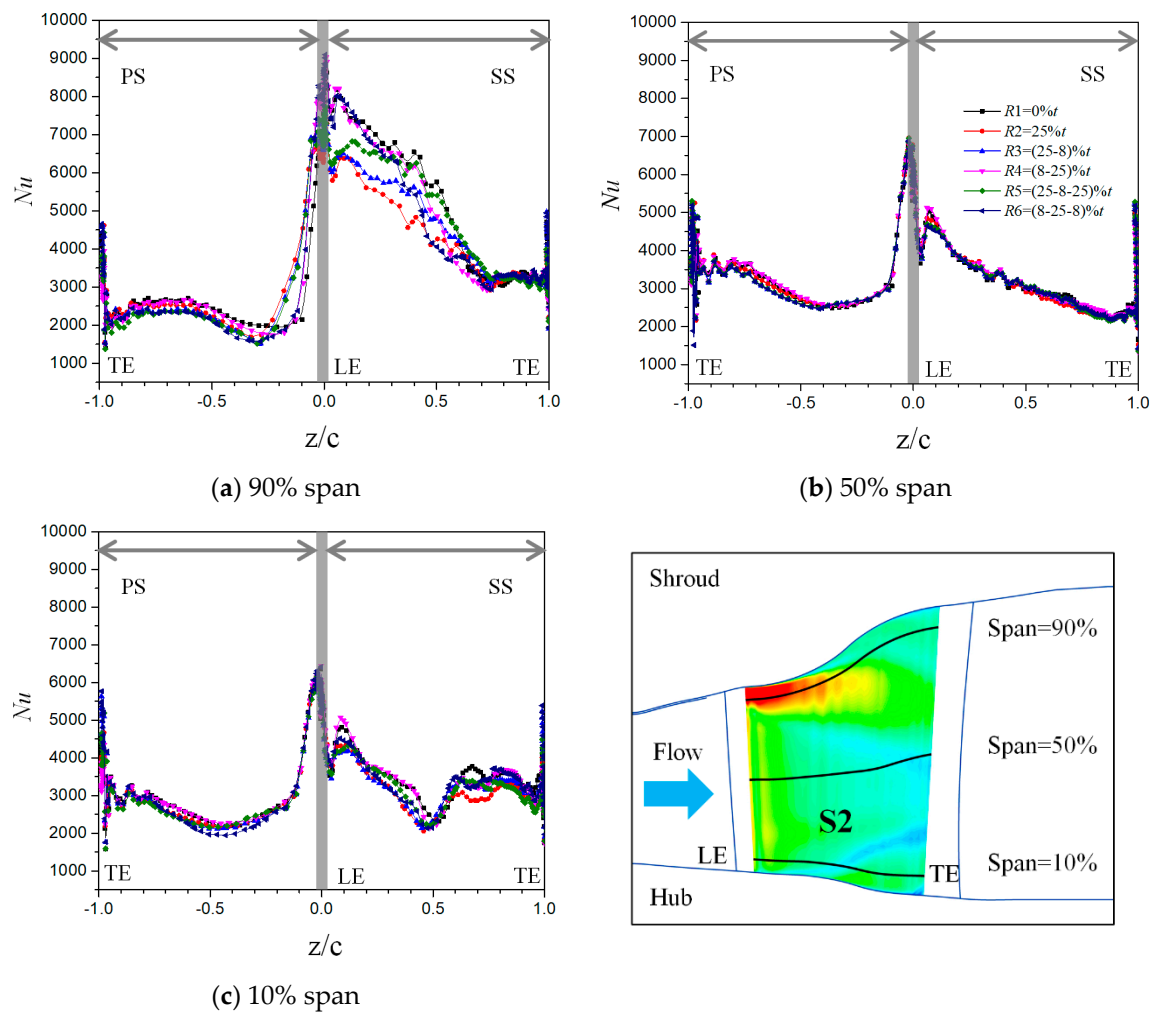

Figure 16. *Nu* distribution for S2 at 1% span (**a**), 50% span (**b**), and 99% span (**c**) blade.

3.3. Comparison of Aerodynamic and Heat Transfer Performance of S2

Table 4 shows the influence of fillet structure on the overall aerodynamic performance parameters and thermal load parameters of the S2 blade. For the loss coefficient, C_p, no matter what form of fillet structure is adopted, it will be conducive to the improvement of the overall flow state of the S2 with a large meridional expansion endwall. In the case of $R3$, it can be seen that the leading edge is filleted with an appropriate large radius ($R = 25\%\ t$) and the trailing edge is filleted with an appropriate small radius ($R = 8\%\ t$), so as to minimize the loss coefficient of the S2 and reduce 0.8% for the case without fillet. By comparing cases $R2$ and $R3$, it can be concluded that a small-radius fillet at trailing edge is conducive to improving the flow state. Correspondingly, by comparing cases $R2$ and $R4$, it can be concluded that a large-radius fillet at the leading edge is conducive to improving the flow state. The total thermal load can be reflected by the area-averaged heat flux. It can be seen that the thermal load of shroud and blade decreases with the fillet structure. Area-averaged shroud heat flux is reduced

by 3.1% by using the fillet distribution of *R*3. Use case R2's fillet radius distribution, reducing the area-averaged blade heat flux by 2.7%. Therefore, it can be concluded that the use of the large leading edge radius fillet and the small trailing edge radius fillet is conducive to the improvement of the flow state and the reduction of the overall thermal load of the large meridional expansion turbine.

Table 4. Loss Coefficient and area-averaged Shroud/Blade Heat Flux.

Case	C_p	Area-Averaged Shroud Heat Flux (w/m^2)	Area-Averaged Blade Heat Flux (w/m2)
$R1 = 0\%\ t$	0.135743	465,863	480,512
$R2 = 25\%\ t$	0.129324	462,693	465,802
$R3 = (25–8)\%\ t$	0.127721	454,382	467,598
$R4 = (8–25)\%\ t$	0.13342	463,625	472,427
$R5 = (25 –8–25)\%\ t$	0.131389	462,550	469,499
$R6 = (8–25–8)\%\ t$	0.131663	460,239	478,626

4. Conclusions

In this paper, a 1.5-stage large meridional expansion turbine was numerically simulated, and the influence of the fillet structures on the flow and heat transfer of the large meridional expansion vane under the influence of upstream wakes and leakage vortices was analyzed. The results show that the flow performance of the large meridional expansion vane can be improved and the thermal load can be reduced by proper arrangement of fillet radius.

1. The fillet structure with the concave surface property at the leading edge of the blade can reduce the strength of the adverse pressure gradient on the suction surface of the leading edge. This is mainly achieved by increasing the radial position of the leading edge horseshoe vortex.
2. An increase in the fillet radius of the leading edge within a reasonable range will reduce the adverse pressure gradient strength of the suction surface, and the strength of the pressure surface branches of the horseshoe vortex and the passage vortex can be reduced. Contrary to the influence of the leading edge, a smaller fillet radius at the trailing edge can reduce the intensity of the trailing edge vortex and the shed vortex near the endwall.
3. The effect of fillet structure on wall thermal load is consistent with that on flow performance. The large fillet radius at the leading edge of the blade can significantly reduce the high thermal load of the endwall and the suction surface of the blade. The small fillet radius can reduce the high thermal load caused by the shed vortex at the trailing edge.
4. Based on comprehensive analysis, it is found that the structure with the large fillet radius at the leading edge and the small fillet radius at the trailing edge is conducive to improving flow performance and reducing the high thermal load for the vane of the large meridional expansion turbine.

Author Contributions: Investigation, validation, writing—original draft, and writing—review and editing were made by F.M.; Project administration was made by Q.Z.; Software and validation were made by J.Z.

Conflicts of Interest: The authors declare no conflict of interest.

Nomenclature

Romans and Greeks

Nu	= Nusselt number
p	= pressure, kPa
q	= heat flux, kW/m^2
T	= temperature, K
T_{aw}	= adiabatic wall temperature, K
T_g	= gas temperature, K
T_w	= isothermal wall temperature, K
u	= velocity, m/s
T_{01}	= inlet temperature, K
Ω	= rotation tensor
S	= strain tensor
C	= vane midspan true chord
k	= thermal conductivity
$\bar{p}_{t,out}$	= average relative total pressure at the outlet, kPa
$\bar{p}_{t,in}$	= average relative total pressure at the inlet, kPa
p_t	= local relative total pressure, kPa
$\bar{p}_{s,out}$	= average static pressure at the outlet, kPa
C_{ps}	= static pressure coefficient
C_p	= total pressure loss coefficient
R	= fillet radius
Yp	= relative total pressure loss coefficient

Subscripts, Superscripts, Abbreviations

R1	= first rotor
S1	= first stator
S2	= second stator
Exp	= experimental
PS, SS	= pressure side, suction side
CFD	= Computational Fluid Dynamics
HTC	= Heat Transfer Coefficient
SST	= shear stress transport
TLV	= tip-leakage vortex
SV	= shed vortex
RANS	= Reynolds-Averaged Navier-Stokes
LE	= leading edge
TE	= trailing edge

References

1. Wei, Z.J.; Qiao, W.Y.; Liu, J.; Duan, W.H. Reduction of endwall secondary flow losses with leading-edge fillet in a highly loaded low-pressure turbine. *Proc. Inst. Mech. Eng. Part A* **2016**, *230*, 184–195. [CrossRef]
2. Ananthakrishnan, K.; Govardhan, M. Influence of fillet shapes on secondary flow field in a transonic axial flow turbine stage. *Aerosp. Sci. Technol.* **2018**, *82*, 425–437. [CrossRef]
3. Sharma, O.P.; Butler, T.L. Predictions of endwall losses and secondary flows in axial flow turbine cascades. *J. Turbomach.* **1987**, *109*, 229–236. [CrossRef]
4. Zess, G.A.; Thole, K.A. Computational design and experimental evaluation of using a leading edge fillet on a gas turbine vane. *J. Turbomach.* **2002**, *124*, 167–175. [CrossRef]
5. Becz, S.; Majewski, M.S.; Langston, L.S. Leading edge modification effects on turbine cascade endwall loss. In Proceedings of the ASME Turbo Expo 2003 collocated with the 2003 International Joint Power Generation Conference, Atlanta, GA, USA, 16–19 June 2003; ASME: New York, NY, USA, 2003; pp. 359–367.
6. Sauer, H.; Muller, R.; Vogeler, K. Reduction of secondary flow losses in turbine cascades by leading edge modifications at the endwall. *J. Turbomach.* **2001**, *123*, 207–213. [CrossRef]

7. Gregory-Smith, D.; Bagshaw, D.; Ingram, G.; Stokes, M. Using profiled endwalls, blade lean and leading edge extensions to minimize secondary flow. In Proceedings of the ASME Turbo Expo 2008: Power for Land, Sea, and Air, Berlin, Germany, 9–13 June 2008; ASME: New York, NY, USA, 2008; pp. 1301–1311.

8. Shi, Y.; Li, J.; Feng, Z.P. Influence of rotor blade fillets on aerodynamic performance of turbine stage. In Proceedings of the ASME Turbo Expo 2010: Power for Land, Sea, and Air, Glasgow, UK, 14–18 June 2010; ASME: New York, NY, USA, 2010; pp. 1657–1668.

9. Pieringer, P.; Sanz, W. Influence of the fillet between blade and casing on the aerodynamic performance of a transonic turbine vane. In Proceedings of the ASME Turbo Expo 2004: Power for Land, Sea, and Air, Vienna, Austria, 14–17 June 2004; ASME: New York, NY, USA, 2004; pp. 1045–1052.

10. Lin, A.Q.; Sun, Y.G.; Zhang, H.; Lin, X.; Yang, L.; Zheng, Q. Fluctuating characteristics of air-mist mixture flow with conjugate wall-film motion in a compressor of gas turbine. *Appl. Therm. Eng.* **2018**, *142*, 779–792. [CrossRef]

11. Mahmood, G.I.; Acharya, S. Experimental investigation of secondary flow structure in a blade passage with and without leading edge fillets. *J. Fluids Eng.* **2007**, *129*, 253–262. [CrossRef]

12. Shih, T.I.P.; Lin, Y.L. Controlling secondary-flow structure by leading-edge airfoil fillet and inlet swirl to reduce aerodynamic loss and surface heat transfer. In Proceedings of the ASME Turbo Expo 2002: Power for Land, Sea, and Air, Amsterdam, The Netherlands, 3–6 June 2002; ASME: New York, NY, USA, 2002; pp. 1023–1032.

13. Mahmood, G.I.; Acharya, S. Measured endwall flow and passage heat transfer in a linear blade passage with endwall and leading edge modifications. In Proceedings of the ASME Turbo Expo 2007: Power for Land, Sea, and Air, Montreal, QC, Canada, 14–17 May 2007; ASME: New York, NY, USA, 2007; pp. 917–930.

14. Han, S.; Goldstein, R.J. Influence of blade leading edge geometry on turbine endwall heat (mass) transfer. In Proceedings of the ASME Turbo Expo 2005: Power for Land, Sea, and Air, Reno, NV, USA, 6–9 June 2005; ASME: New York, NY, USA, 2005; pp. 547–561.

15. Han, S.; Goldstein, R.J. The heat/mass transfer analogy for a simulated turbine endwall with fillets. *J. Heat Transf.* **2009**, *131*, 012001. [CrossRef]

16. Meng, F.S.; Zheng, Q.; Gao, J.; Fu, W.L. Effect of tip clearance on flow field and heat transfer characteristics in a large meridional expansion turbine. *Energies* **2019**, *12*, 162. [CrossRef]

17. Fu, W.L.; Gao, J.; Liang, C.; Wang, F.K.; Zheng, Q.; Zhou, E.D. Experimental Investigation on the Annular Sector Cascade of a High Endwall-Angle Turbine. In Proceedings of the ASME Turbo Expo 2016: Turbomachinery Technical Conference and Exposition, Seoul, Korea, 13–17 June 2016; ASME: New York, NY, USA, 2016.

18. Qureshi, I.; Smith, A.D.; Povey, T. Hp vane aerodynamics and heat transfer in the presence of aggressive inlet swirl. *J. Turbomach.* **2013**, *135*, 021040. [CrossRef]

19. Ameri, A.A.; Steinthorsson, E.; Rigby, D.L. Effect of squealer tip on rotor heat transfer and efficiency. *J. Turbomach.* **1998**, *120*, 753–759. [CrossRef]

20. AEA Technology. *ANSYS CFX User Documentation*; AEA Technology: Harwell, UK, 2006.

21. Krishnababu, S.K.; Newton, P.J.; Dawes, W.N.; Lock, G.D.; Hodson, H.P.; Hannis, J.; Whitney, C. Aero-thermal investigations of tip leakage flow in axial flow turbines: Part I—Effect of tip geometry and tip clearance gap. In Proceedings of the ASME Turbo Expo 2007: Power for Land, Sea, and Air, Montreal, QC, Canada, 14–17 May 2007; ASME: New York, NY, USA, 2007; pp. 727–738.

22. Zuckerman, N.; Lior, N. Impingement heat transfer: Correlations and numerical modeling. *J. Heat Transf.* **2005**, *127*, 544–552. [CrossRef]

23. Bonelli, F.; Viggiano, A.; Magi, V. A numerical analysis of hydrogen underexpanded jets. In Proceedings of the Internal Combustion Engine Division Spring Technical Conference, Torino, Piemonte, Italy, 6–9 May 2012; p. ICES2012–81068.

24. Luo, J.; Razinsky, E.H. Prediction of heat transfer and flow transition on transonic turbine airfoils under high freestream turbulence. In Proceedings of the ASME Turbo Expo 2008: Power for Land, Sea, and Air, Berlin, Germany, 9–13 June 2008; ASME: New York, NY, USA, 2008; pp. 1301–1310.

25. Montomoli, F.; Adami, P.; Martelli, F. A finite-volume method for the conjugate heat transfer in film cooling devices. *Proc. Inst. Mech. Eng. Part A* **2009**, *223*, 191–200. [CrossRef]

26. Marchal, P.; Sieverding, C.H. Secondary flows within turbomachinery bladings. In *Secondary Flows in Turbomachines, AGARD-CP-214*; AGARD, Ed.; Harford House: London, UK, 1977; pp. 1–11.

27. Benner, M.W.; Sjolander, S.A.; Moustapha, S.H. Measurements of secondary flows in a turbine cascade at off-design incidence. In Proceedings of the ASME 1997 International Gas Turbine and Aeroengine Congress and Exhibition, Orlando, FL, USA, 2–5 June 1997; ASME: New York, NY, USA, 1997; pp. 1–10.
28. Simone, S.; Montomoli, F.; Martelli, F.; Chana, K.S.; Qureshi, I.; Povey, T. Analysis on the effect of a nonuniform inlet profile on heat transfer and fluid flow in turbine stages. *J. Turbomach.* **2012**, *134*, 011012. [CrossRef]